www.MaterialsViews.com

Catalysts

Graphene-Supported Mesoporous Carbons Prepared with Thermally Removable Templates as Efficient Catalysts for Oxygen Electroreduction

Wenhan Niu, Ligui Li, Ji Liu, Nan Wang, Wei Li, Zhenghua Tang, Weijia Zhou, and Shaowei Chen**

Graphene-supported mesoporous carbons with rich nitrogen self-doped active sites (N-MC/rGO) are prepared by direct pyrolysis of a graphene-oxide-supported polymer composite embedded with massive, evenly distributed amorphous FeOOH that serve as efficient thermally removable templates. The resulting N-MC/rGO catalysts exhibit high surface areas and apparent electrocatalytic activity for oxygen reduction reaction in alkaline media. Among the series, the sample prepared at 800 °C displays the best performance with a more positive onset potential, higher limiting currents, much higher stability, and stronger poison resistance than commercial Pt/C. This is ascribed to the synergetic functions of the highly conductive graphene support and the mesoporous N-doped carbons that effectively impede the restacking of the graphene sheets and enhance the exposure of the rich nitrogen self-doped active sites.

1. Introduction

With a remarkable efficiency and high-energy density, polymer exchange membrane fuel cells (PEMFCs) have been hailed as a green technology that meets the energy requirements to power future electrical vehicles, portable electronics, and other energy-consuming devices. Oxygen reduction reaction (ORR) represents a critical reaction process at the fuel cell cathode. Because of the complex reaction pathways and sluggish electron-transfer kinetics, a large quantity of noble metals (e.g., Pt and Pd) and their alloys are generally needed to effectively catalyze the reaction so that a sufficiently high current density can be generated for practical applications. However, to achieve large-scale commercialization of PEMFCs, several important issues need to be addressed simultaneously: low catalytic activity, high costs, and low stability of noble metals-based catalysts.[1] Consequently, developing cost-effective alternatives with competitive catalytic activity and long stability for ORR has been a foremost issue in PEMFCs.[2]

Recent studies have shown that heteroatom-doped (N, B, P, etc.) carbon-based nanomaterials may serve as efficient, low-cost alternatives to Pt for ORR.[3] Of these, graphene nanosheets have received intensive attention, mainly due to their high electrical conductivity, ultra-large specific surface area, and strong resistance to oxidation at high potentials, as compared with the commonly used carbon black.[4] Therefore, in the preparation of carbon-based ORR catalysts, maximizing graphitization is typically desired. Currently, graphene nanosheets are mostly prepared via the modified Hummers method,[5] where graphene oxide (GO) sheets are first obtained by chemical exfoliation of graphite precursors and then reduced by strong reducing agents such as hydrazine and $NaBH_4$, or high temperature heating to

W. H. Niu, Prof. L. G. Li, J. Liu, N. Wang, W. Li, Prof. Z. H. Tang, Prof. W. J. Zhou, Prof. S. W. Chen
New Energy Research Institute
College of Environment and Energy
South China University of Technology
Guangzhou 510006, China
E-mail: esguili@scut.edu.cn; shaowei@ucsc.edu
Prof. S. W. Chen
Department of Chemistry and Biochemistry
University of California
1156 High Street, Santa Cruz, CA 95064, USA

DOI: 10.1002/smll.201503542

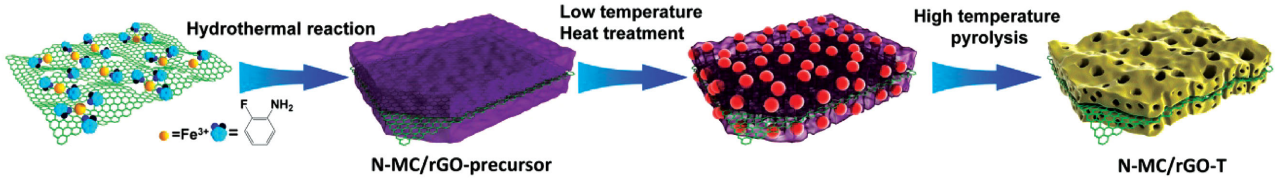

Scheme 1. Schematic illustration of the preparation process of N-MC/rGO-*T* catalysts.

restore the Csp^2 honeycomb-like lattice. However, during the reduction, graphene nanosheets tend to restack/aggregate because of the large-area, strong π–π interactions and thus decrease the effective electrochemical surface area that is of paramount significance in catalysis. To minimize restacking of graphene sheets, several methods have been reported in the literature.[6] Of these, deposition of porous carbon derived from intrinsic porous polymers onto the surface of graphene represents an effective route.[6c,d] This method usually involves multiple organic synthesis/polymerization processes. Unfortunately, direct carbonization of the porous polymer/graphene precursors generally results in severe diminishment of the surface area due to collapse of pores at high temperatures. Conventionally, rigid templates such as nanostructured SiO_2, ZnO, and Al_2O_3 have been added to reduce pore collapse during the carbonization process.[7] However, this complicates the synthetic procedure, as it involves time- and energy-consuming processes for the a priori synthesis of the templates and post-synthesis removal of excess templates, neither of which is beneficial for mass production. In addition, the catalytic activity may be compromised because part of the active sites may be inevitably lost in the post-synthesis removal of excess templates by acid/base etching. Therefore, it remains challenging and yet desired to develop facile and effective strategies for the preparation of graphene-based porous carbons with a high surface area.

Herein, we used the method based on thermally removable templates that we recently developed[8] to prepare graphene-supported mesoporous carbons (N-MC/rGO) with rich nitrogen self-doped active sites and large specific surface areas by direct carbonization of polymer/graphene oxide hybrid precursors without any post-synthesis treatments. In alkaline media, the obtained nanocomposites exhibited a remarkable ORR activity, with the best catalyst featuring a more positive onset potential (+0.99 V vs reversible hydrogen electrode (RHE)) and half-wave potential (+0.83 V), much higher diffusion-limited current and kinetic current, larger electron-transfer number (n > 3.95) even at low overpotentials, and stronger tolerance to methanol than state-of-the art commercial Pt/C catalysts. In particular, the incorporation of graphene nanosheets endowed the catalysts with substantially enhanced stability, making it much more stable than Pt/C and porous carbons alone.

2. Results and Discussion

In the preparation of N-MC/rGO hybrids (**Scheme 1**), a precursor was first synthesized by hydrothermal polymerization of 2-fluoroaniline initiated by $FeCl_3$ in an aqueous dispersion of GO nanosheets. The precursor exhibited a sheet-like morphology with a rough surface, as evidenced in scanning electron microscopic (SEM) measurements (Figure S1a,b, Supporting Information). This suggests that poly(2-fluoroaniline) (P2FANI) was formed and deposited onto the GO nanosheets probably due to the strong π–π interactions between P2FANI and the graphene planes. Consistent results were obtained in transmission electron microscopic (TEM) measurements and elemental mapping based on energy dispersive X-ray spectroscopy (EDS). As depicted in **Figure 1**a,b, the N-MC/rGO-precursor exhibited a sheet-like structure covered with a rough overlayer of a somewhat darker contrast. EDS mapping analysis (Figure 1c) showed that the elements of Fe, N, C, F, and Cl were distributed homogeneously within the sample. Interestingly, although a high content of Fe (1.62 at%, based on X-ray photoelectron spectroscopic (XPS) analysis; Table S1, Supporting Information) was found within the precursor, no Fe-containing nanoparticle could be identified even in high-resolution TEM studies. In fact, X-ray diffraction (XRD) studies (Figure S2, Supporting Information) showed only two broad diffraction peaks centered at $2\theta \approx 25°$ and 44°, corresponding to the diffractions of the (002) and (101) lattice planes of typical turbostratic carbon. No other diffraction peak can be resolved, signifying that the Fe-containing compounds in the precursors were actually amorphous. High-resolution XPS measurements of the Fe2p electrons (Figure S3, Supporting Information) revealed two main peaks centered at 711.0 eV ($Fe2p_{3/2}$) and 724.8 eV ($Fe2p_{1/2}$), along with two satellite peaks at 718.3 and 731.4 eV, which were consistent with those of FeOOH,[9] indicating the formation of amorphous FeOOH in N-MC/rGO-precursor. This is further confirmed by results of the O1s electrons (Figure S4, Supporting Information) and the Fe3p electrons (Figure S5, Supporting Information).[10] Taking all these into account, one can see that 2-fluoroaniline likely served as a complexing ligand to thoroughly coordinate with Fe^{3+} during the polymerization process, and consequently Fe^{3+} was evenly distributed in the resulting P2FANI matrix.

The precursors then underwent high-temperature pyrolysis to produce N-MC/rGO-*T* (Scheme 1). Figure 1d,e shows the TEM images of the sample prepared by pyrolysis at 800 °C for 2 h, where one can see that the planus nanosheets of the N-MC/rGO-precursor became markedly crumpled (Figure S1c,d, Supporting Information). Elemental mapping studies (Figure 1f) showed high contents of C and N that were distributed rather evenly within the sample; however, the signals of F, Cl, and Fe were virtually undetectable, indicating that the polymer matrix was effectively carbonized, and FeOOH had been almost completely removed, with the formation of a small number of Fe_3O_4 nanoparticles

www.MaterialsViews.com

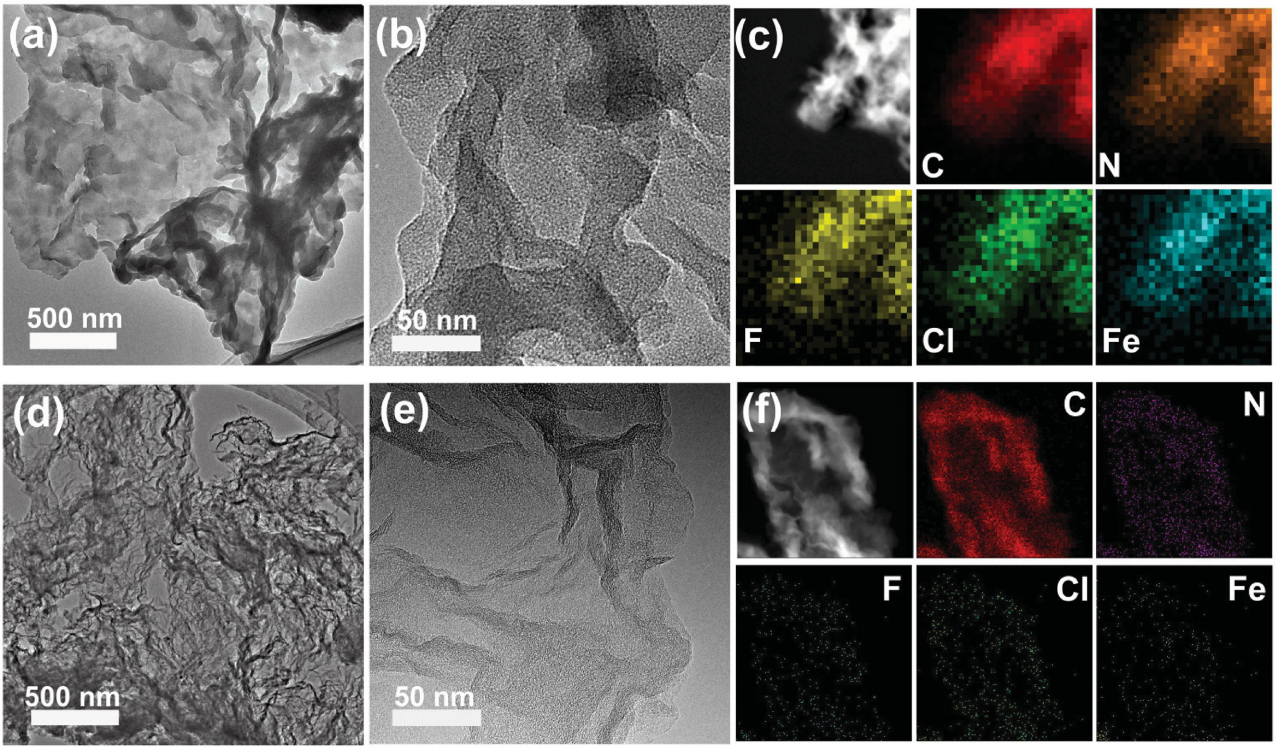

Figure 1. a,b,d,e) TEM images and c,f) selected-area elemental maps of a–c) N-MC/rGO precursor and d–f) N-MC/rGO-800, respectively.

(Figure S6, Supporting Information), as manifested in XRD measurements. From **Figure 2**a, clearly defined diffraction peaks can be seen at 18.3°, 30.1°, 35.4°, 37.1°, 43.0°, 53.5°, 57.0°, and 62.6° with all N-MC/rGO-*T* (*T* = 700, 800, and 900) samples, which are consistent with the (111), (220), (311), (222), (400), (422), (511), and (440) lattice planes of Fe_3O_4 (JCPDS card No. 65-3107), respectively. Thermogravimetric analysis (TGA) in an O_2 atmosphere showed that Fe_3O_4

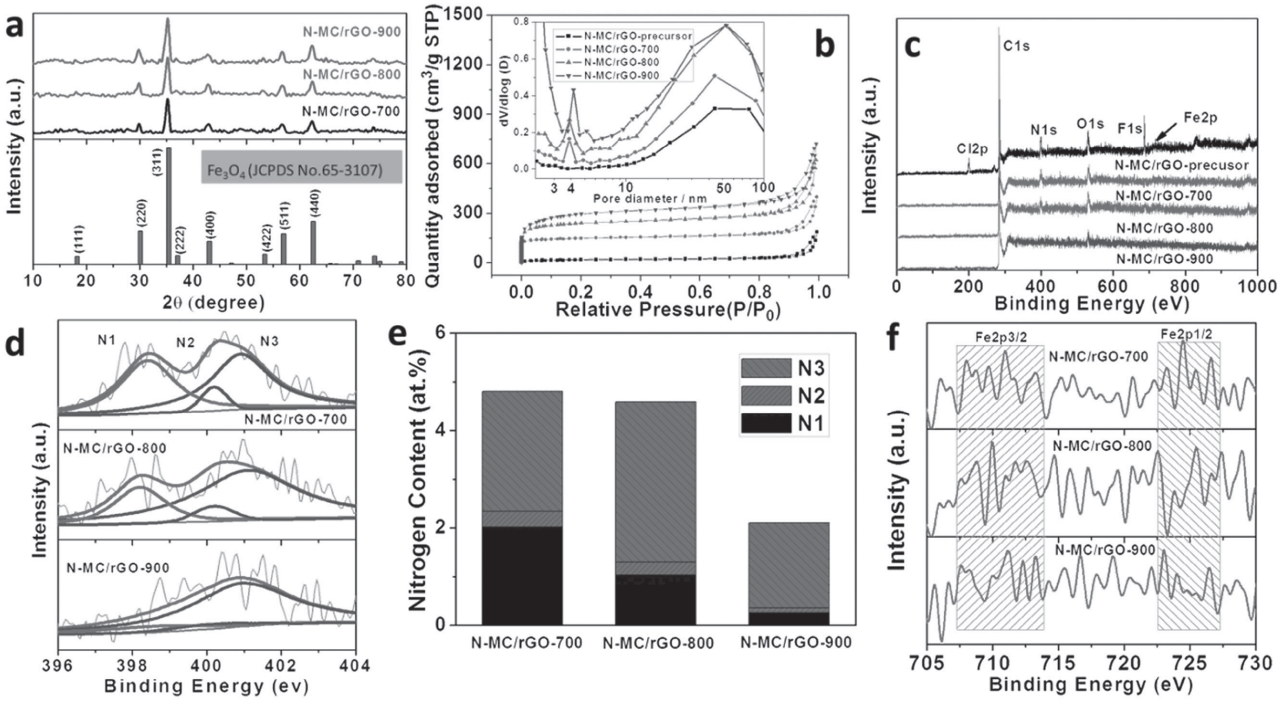

Figure 2. a) XRD patterns. b) BET surface area (inset is the pore size distribution). c) XPS survey spectra of N-MC/rGO-precursor and N-MC/rGO-*T* (*T* = 700, 800, 900). d) High-resolution XPS spectra of N1s electrons (black curves are the experimental data and the colored curves are deconvolution fits). e) concentrations of different N dopants. f) Fe2p spectra of the N-MC/rGO-*T* samples.

accounted for 13.5%, 17.28%, and 19.8% in weight in N-MC/rGO-700, N-MC/rGO-800, and N-MC/rGO-900, respectively (Figure S7, Supporting Information).

Brunauer–Emmet–Teller (BET) analyses were then conducted to investigate the specific areas and pore sizes of these samples. The results showed that the samples were highly mesoporous with high surface areas. As shown in Figure 2b, the apparent surface area was only 65 m^2 g^{-1} for the N-MC/rGO-precursor; yet after pyrolysis, it increased markedly to about 501 m^2 g^{-1} for N-MC/rGO-700, 821 m^2 g^{-1} for N-MC/rGO-800, and even 1038 m^2 g^{-1} for N-MC/rGO-900. This is in sharp contrast to previous reports where pyrolysis at elevated temperatures (>800 °C) usually led to collapse of pores in catalysts, signifying that the graphene substrates effectively preserved the pore structure in the hybrids. Furthermore, the pore-size distribution indicates the formation of mesopores of 4–50 nm in diameter (inset to Figure 2b) in the N-MC/rGO-*T* samples, which are known to facilitate the mass transport of ORR-relevant species (OH^-, H_2O, O_2, etc.) and hence enhance the ORR catalytic activity.[4c] Note that the specific areas of the N-MC/rGO-800 and 900 samples are markedly higher than those of graphene-based catalysts reported in the literature,[6f,11] implying better exposure of active sites that might enhance the catalytic performance (vide infra).

To understand the impacts of pyrolysis temperature on the formation of mesopores in the N-MC/rGO catalysts, two additional samples were prepared in a similar fashion but at lower pyrolysis temperatures of 300 and 500 °C (denoted as N-MC/rGO-300 and N-MC/rGO-500, respectively). In comparison with N-MC/rGO-precursor where no particulate feature was observed (Figure S8a, Supporting Information), the N-MC/rGO-300 sample showed a small number of nanoparticles (Figure S8b, Supporting Information), whereas a large number of nanoparticles were found embedded in the P2FANI matrix of the N-MC/rGO-500 sample (Figure S8c, Supporting Information). In the corresponding XRD patterns (Figure S8d, Supporting Information), the N-MC/rGO-300 sample showed only a single broad peak centered at $2\theta \approx 25°$ that was assigned to the porous carbons, which indicated that the aggregates were likely the hybrids of GO and amorphous FeOOH. In contrast, the XRD patterns of N-MC/rGO-500 revealed well-defined Fe_3O_4 diffraction peaks, which suggested that the amorphous FeOOH had been transformed into Fe_3O_4 crystals at 500 °C. These nanoparticles then acted as rigid templates to prevent the collapse of the polymer matrix and were concurrently removed by conversion into volatile compounds during high-temperature carbonization. In fact, after pyrolysis at elevated temperatures (700–900 °C), the solids condensed on the low-temperature end of the tubular furnace (away from the porous carbons) were collected and dissolved in water. When 0.01 M KSCN was added dropwise into the solution, one can see that the colorless solution gradually became bloody red (Figure S9a, Supporting Information), a typical color of $K_3[Fe(SCN)_6]$, which clearly demonstrates that Fe in the polymer matrix was removed by the formation of volatile Fe-containing compounds. Considering the elemental compositions of the N-MC/rGO-precursor (Table S1, Supporting Information), the volatile Fe-containing compound is most likely $FeCl_2$ and $FeCl_3$. In addition, when the end gas released from pyrolysis of the N-MC/rGO-precursor was introduced into a clear limewater solution, white precipitates were produced gradually (Figure S9b, Supporting Information), indicating the formation of CO_2. TGA measurements were also conducted to further monitor the carbonization process. As shown in Figure S10 (Supporting Information), the TGA curve depicted four major weight-loss steps in N_2. The sudden weight loss of ≈56% starting at about 700 °C was attributed to the formation of a large quantity of volatile compounds such as CO, CO_2, $FeCl_2$, $FeCl_3$, and HF (Figure S10, Supporting Information) due to the decomposition of the polymer and the Fe_3O_4 nanoparticles derived from FeOOH, which helped produce a number of cavities/holes in the carbon matrix,[8,12] as shown in Scheme 1.

The carbonization of the polymer matrix was confirmed by Raman measurements where the graphitic D and G bands can be clearly seen at ≈1347 and 1590 cm^{-1}, respectively, for all examples (Figure S11, Supporting Information). In addition, the ratio of the D and G band intensities (I_D/I_G) of the nanocomposites varied slightly with the pyrolysis temperature at 0.94 for N-MC/rGO-700, 0.97 for N-MC/rGO-800, and 1.04 for N-MC/rGO-900. That is, with an increase of the pyrolysis temperature from 700 to 900 °C, the I_D/I_G ratio increased slightly, suggesting a somewhat decreasing order of the graphitic carbons, probably due to the incorporation of nitrogen dopants into carbon matrix that disturbed the sp^2 carbon network of the mesoporous carbons.[13]

The elemental compositions of the samples were then quantitatively assessed by XPS measurements. In the survey spectra (Figure 2c), the Cl 1s, F1s, and Fe2p peaks were clearly defined in the N-MC/rGO-precursor. However, pyrolysis at elevated temperatures (700–900 °C) led to complete removal of Cl and F, leaving only N, C, O, and a trace amount of Fe in the N-MC/rGO-*T* (*T* = 700, 800, 900) samples (Table S1, Supporting Information). Furthermore, the N1s spectra (Figure 2d) can be deconvoluted into three peaks at (N1) 398.4 ± 0.2, (N2) 400.1 ± 0.1, and (N3) 401.0 ± 0.1 eV, which are assigned to pyridinic N, pyrrolic N, and graphitic N (Figure S12, Supporting Information), respectively.[6c,14] This indicates that nitrogen was indeed successfully self-doped into the carbon molecular skeletons. In addition, based on the integrated peak areas, the concentrations of the different nitrogen dopants were quantified (Figure 2e), where it can be seen that graphitic N and pyridinic N were the dominant species in the N-MC/rGO-700, N-MC/rGO-800, and N-MC/rGO-900 samples, and the highest content of graphitic N was observed at 3.29 at% for N-MC/rGO-800, as compared to 2.47 at% for N-MC/rGO-700 and 1.74 at% for N-MC/rGO-900, whereas the total concentrations of the three nitrogen dopants combined decreased markedly with increasing pyrolysis temperature (Table S1, Supporting Information). Furthermore, the Fe2p electrons (Figure 2f) can be identified at 707–713 eV ($Fe2p_{3/2}$) and 722–727 eV ($Fe2p_{1/2}$), and the Fe atomic fraction was found to decrease from 1.62 at% for the N-MC/rGO-precursor sample to only 0.86 at% for N-MC/rGO-700, 0.80 at% for N-MC/rGO-800, and 0.36 at% for N-MC/rGO-900 (Table S1, Supporting Information). This observation is in good agreement with the results in EDS

elemental mappings (Figure 1f) and large-area EDS analysis (Figure S13, Supporting Information) where the Fe element was almost completely removed, most likely through the formation of volatile iron compounds during pyrolysis (Figure S10, Supporting Information).

Note that it has been argued that pyridinic N may coordinate with Fe to form Fe-N_x species and serve as active sites for ORR;[15] in addition, graphitic N dopants can help facilitate the adsorption of oxygen molecules on adjacent carbon atoms, the rate determining step in ORR.[16] In fact, the N-MC/rGO porous carbons obtained above exhibited remarkable ORR activity in alkaline media. Whereas only featureless double-layer charging currents were observed in N_2-saturated 0.1 M KOH within the potential range of –0.04 to +1.16 V for all samples (Figure S14, Supporting Information), a clear cathodic peak appeared when the solution was saturated with O_2, with the peak potential at +0.65 V for N-MC/rGO-700, +0.80 V for N-MC/rGO-800, and +0.79 V for N-MC/rGO-900. This suggests apparent ORR activity of the porous carbons. For the N-MC/rGO-800 catalyst, the oxygen reduction peak appeared at almost the same potential position as that of Pt/C, and was the best among the series.

Figure 3a depicts the rotating disk electrode (RDE) voltammograms for the N-MC/rGO-*T* samples in an O_2-saturated 0.1 M KOH solution. For the N-MC/rGO-700 sample, an abrupt increase of cathodic current appeared when the electrode potential was swept negatively past +0.90 V (vs RHE); for N-MC/rGO-900 and Pt/C, the onset potential was much more positive at +0.96 and +0.98 V, respectively, indicating that a lower overpotential was needed to trigger ORR on both catalysts. For N-MC/rGO-800, it was even more positive at +0.99 V, demonstrating the lowest overpotential for ORR among the series. Moreover, the limiting current of N-MC/rGO-800 was also the highest. For instance, at +0.40 V, the limiting current was 5.86 mA cm^{-2} for N-MC/rGO-800, which is markedly higher than that of N-MC/rGO-700 (3.48 mA cm^{-2}), N-MC/rGO-900 (4.00 mA cm^{-2}), and even Pt/C at an optimized loading (204 μg cm^{-2}, 5.10 mA cm^{-2}) (see Figure S15 in the Supporting Information). These observations clearly show that the N-MC/rGO-800 sample was the best ORR catalyst among the series in the present work. In fact, the ORR activity of N-MC/rGO-800 was even better than the results of most M-N/C catalysts reported in recent studies (Table S2, Supporting Information). Notably, this coincided with the highest total concentrations of graphitic and pyridinic nitrogen in N-MC/rGO-800 (Figure 2e; Table S1, Supporting Information), suggesting that the ORR activity was most likely determined by both kinds of nitrogen dopants as reported in the literature.[6c] In the present work, the superior ORR activity in N-MC/rGO-800 might also result from an optimal balance of the surface area, exposure of active sites, and electrical conductivity.

RRDE experiments were then performed to gain further insights into the ORR kinetics. First, the numbers of electron transfer (n) were estimated by the disk and ring currents (Equation (1)) and depicted in Figure 3b. It can be seen that the n values were all close to 4, indicating that ORR proceeded through a nearly $4e^-$ pathway, although n was slightly higher for the N-MC/rGO-800 sample than for the rest. For instance, at +0.70 V, n = 3.67 for N-MC/rGO-700, 3.95 for N-MC/rGO-800, 3.94 for N-MC/rGO-900, and 3.93 for Pt/C, again, signifying that N-MC/rGO-800 stood out as the best among the series. For the average H_2O_2 yield (Equation (2)), a value of 5.44% was detected over the potential range of

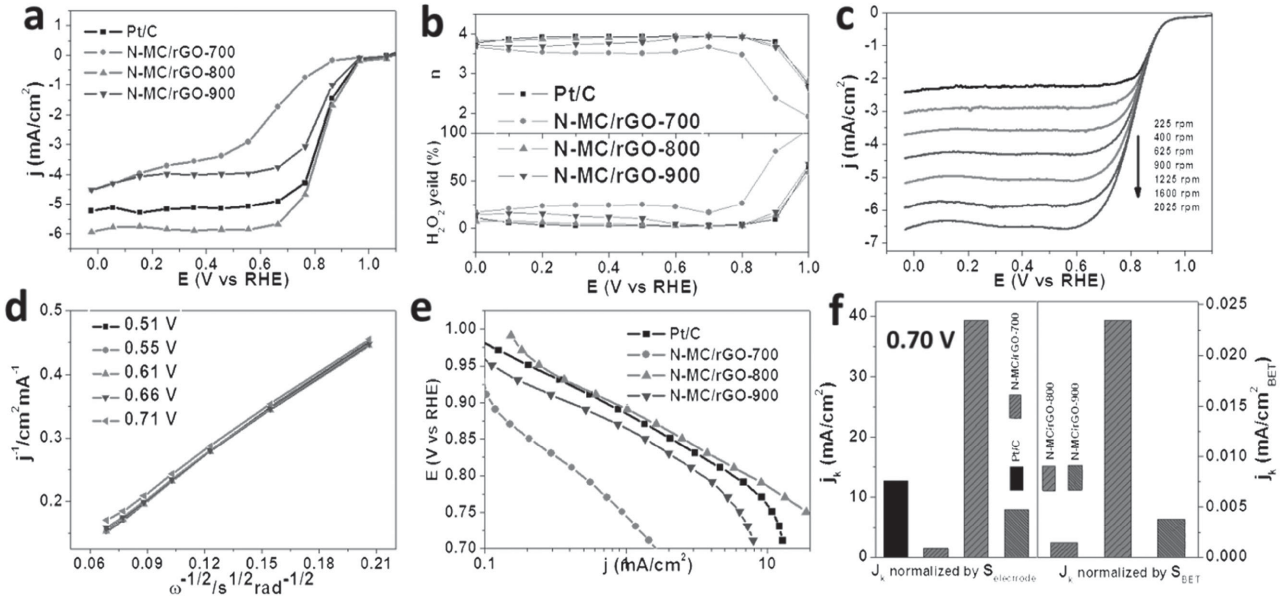

Figure 3. a) RDE voltammograms, and b) plots of hydrogen peroxide yield and electron transfer number of a glassy-carbon electrode modified with 204 μg cm^{-2} of Pt/C (20%) and N-MC/rGO catalysts in an O_2-saturated 0.1 M KOH solution at a rotation speed of 1600 rpm. The potential sweep rate was 10 mV s^{-1}. c) LSV curves for N-MC/rGO-800 at the rotation speeds of 225 to 2025 rpm. d) The corresponding K–L plots for N-MC/rGO-800 at different electrode potentials. e) Tafel plots of Pt/C and N-MC/rGO catalysts. f) Comparison of kinetic current density at +0.70 V. In the left panel, current density was calculated by normalizing kinetic currents to the electrode geometrical surface area, whereas in the right panel, to the respective BET surface area.

0.00 to +0.80 V on the N-MC/rGO-800 electrode, which is the lowest, compared to that of Pt/C (7.60%), N-MC/rGO-700 (21.82%), and N-MC/rGO-900 (9.04%). These results further confirm that the N-MC/rGO-800 is an efficient electrocatalyst for ORR.

From the RDE voltammograms in Figure 3c, one can see that the limiting current of the N-MC/rGO-800 modified electrode increases with increasing rotation speed (from 225 to 2025 rpm). Second, in Koutecky–Levich (K–L) analysis (Figure 3d), one can see that N-MC/rGO-800 exhibited good linearity with a rather consistent slope within the potential range of +0.51 to +0.71 V, suggesting first-order reaction kinetics for ORR in the solution. For the Tafel plots in Figure 3e, in contrast to the large slope observed on N-MC/rGO-700 (92 mV dec^{-1}), a comparable slope was observed for N-MC/rGO-800 (53 mV dec^{-1}), N-MC/rGO-900 (62 mV dec^{-1}), and Pt/C (62 mV dec^{-1}), suggesting a similar reaction mechanism of ORR on the surface of these three catalysts where the rate-determining step was likely the first electron reduction of oxygen. Importantly, within this low overpotential range of +0.70 to +1.00 V, the specific activity of N-MC/rGO-800 was the highest in terms of kinetic current density. Specifically, the kinetic current density (kinetic current normalized to the electrode geometrical surface area, left panel in Figure 3f) obtained from the intercept of the linear K–L plot at +0.70 V (vs RHE) for the N-MC/rGO-800 electrode is 39.3 mA cm^{-2}, while it is only 12.7, 1.4, and 7.9 mA cm^{-2} for Pt/C, N-MC/rGO-700, and N-MC/rGO-900, respectively. It is worthy to note that such a kinetic current density (39.3 mA cm^{-2}) is even higher than the leading results in recent reports,[6c,17] likely due to the high electrical conductivity and high density of exposed active sites in the N-MC/rGO-800 sample.

In fact, electrochemical impedance measurements (Figure S16, Supporting Information) demonstrated that the charge-transfer resistance of N-MC/rGO-800 was the lowest among the N-MC/rGO series, and even lower than that of commercial Pt/C, which coincided with the best ORR performance of the N-MC/rGO-800 samples, as shown above. In addition, the intrinsic resistance of N-MC/rGO-800 was also markedly lower than that without the graphene nanosheet scaffolds (Fe-N/C-800).[8] This clearly shows that the inclusion of graphene nanosheets substantially enhances the electrical conductivity of the catalyst, a critical factor in the determination of the ORR activity.

The kinetic current of the catalysts was also normalized to the respective BET surface area and compared. As shown in the right panel of Figure 3f, at +0.70 V, N-MC/rGO-800 again stood out as the best catalyst among the series, with a current density of 0.023 mA cm^{-2}, about one order of magnitude higher than those of N-MC/rGO-700 (0.0014 mA cm^{-2}) and N-MC/rGO-900 (0.0037 mA cm^{-2}). Note that the BET surface area actually increases in the order of N-MC/rGO-700 < N-MC/rGO-800 < N-MC/rGO-900 (Figure 2b). The fact that the N-MC/rGO-800 sample exhibited the best ORR performance suggests that it contained the highest concentration of accessible active sites.[18]

It should be noted that the nature of the active sites is still a controversial issue for N-doped carbon catalysts derived from Fe-containing precursors. Although it has been argued that Fe is needed for high ORR activity, some propose that Fe only promotes the formation of active sites and does not participate directly in ORR catalysis. Thus, it is crucial to identify the function of the Fe-species in the N-MC/rGO-*T* catalysts. To this end, a series of control experiments were carried out. In the first experiment, KSCN was added into the electrolyte solution and the impacts on the ORR activity of the N-MC/rGO-800 modified glassy-carbon electrode were evaluated by RDE voltammetric measurements. Note that KSCN can strongly coordinate with iron and hence poison the Fe-containing sites for ORR. However, as shown in **Figure 4**a, the RDE voltammogram was virtually unchanged upon the addition of 10×10^{-3} M KSCN into the solution. In the second experiment (Figure 4a), the N-MC/rGO-800 catalyst was first leached in a hot solution of 1.0 M H_2SO_4 for 6 h in order to remove metal (oxide) compounds before being deposited on the glassy-carbon electrode for ORR testing. Interestingly, this leached sample retained the same Fe content (which was almost undetectable; Table S1, Supporting Information), half-wave potential, and diffusion-limiting current as compared to the as-prepared N-MC/rGO-800. Taken together, these results suggest that the trace amounts of Fe_3O_4 nanoparticles were actually encapsulated by the graphene sheets or carbon matrix in the N-MC/rGO-800 catalyst, and their contributions to ORR were minimal. Therefore, it is probable that the ORR catalytic activity of N-MC/rGO-800 arose predominantly determined by the rich N-dopants, especially the graphitic and pyridinic nitrogen (Table S1, Supporting Information). Furthermore, the mesoporous structure is also believed to promote the transport of ORR relevant species, leading to a superior ORR activity.

Resistance of catalysts to methanol crossover is another issue that needs to be addressed for practical applications. As shown in Figure 4b, upon the injection of 3 M methanol into the electrolyte solution, the commercial Pt/C electrode (black curve) showed an abrupt decrease of the voltammetric current. In contrast, the N-MC/rGO-800 electrode maintained the same ORR profile (red curve), suggesting strong tolerance to methanol crossover.

Stability is also an important parameter for catalysts in practical applications. Experimentally, this was assessed by chronoamperometric measurements at +0.70 V in an O_2-saturated 0.1 M KOH solution.[2b,19] To check if the introduction of graphene increased the catalyst durability, mesoporous Fe-N/C-800 sample was also prepared in a similar fashion but without the addition of GO.[8] As shown in Figure 4c, after 22 h of continuous operation, the Pt/C electrode exhibited a rapid decrease of current density with only about 64.3% retention, indicating poor stability of the Pt/C electrode toward ORR; for the Fe-N/C-800 catalyst, about 68.1% of the initial current was retained; in sharp contrast, 85.5% was retained with the N-MC/rGO-800 catalyst under the same testing conditions. This clearly demonstrates that the introduction of graphene significantly enhanced the stability of the N-MC/rGO mesoporous carbon catalysts for ORR.

Cycling test is another method to evaluate the durability of ORR catalysts. By comparing the linear sweep voltammogram (LSV) curves before and after 4500 cycles, one can see that the

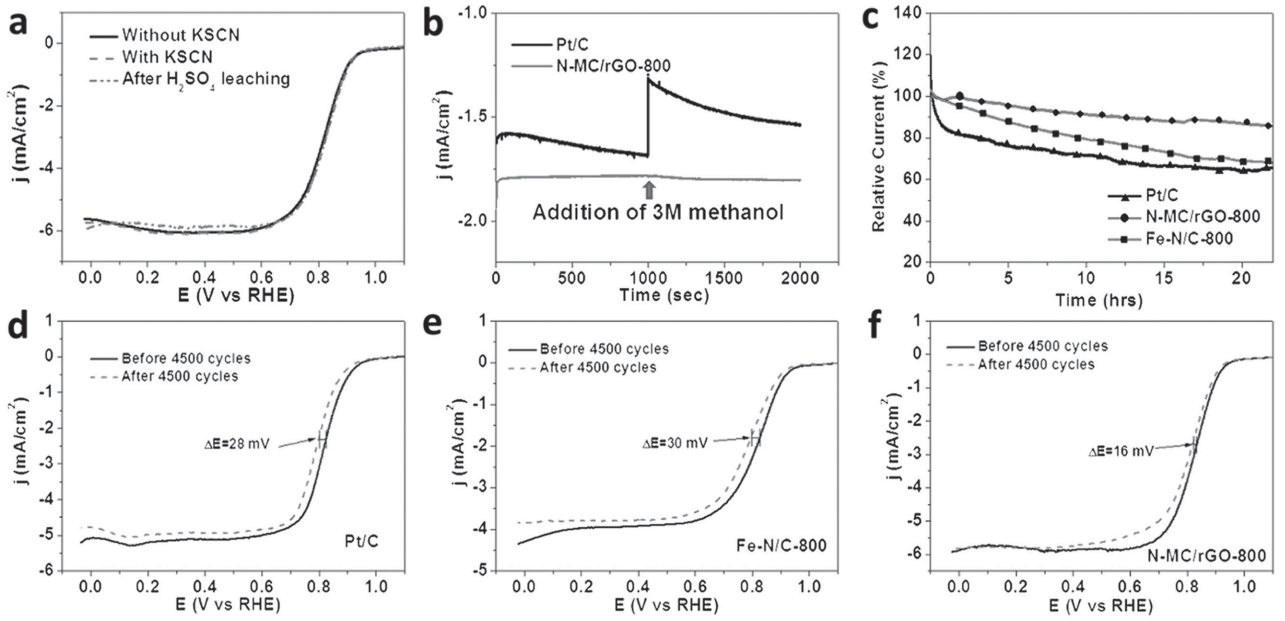

Figure 4. a) LSV curves of N-MC/rGO-800 before and after H_2SO_4 leaching treatments, and in 0.1 M KOH aqueous solution with the addition of 10×10^{-3} M KSCN. Chronoamperometric curves of a glassy-carbon electrode modified with catalysts at +0.70 V versus RHE in b) an O_2-saturated aqueous solution of 0.1 M KOH + 3 M methanol, and c) O_2-saturated 0.1 M KOH solution. The rotation speed was 1225 rpm. LSV curves of d) Pt/C, e) Fe-N/C and f) N-MC/rGO-800 in an O_2-saturated 0.1 M KOH solution before and after 4500 cycles.

N-MC/rGO-800 showed much better durability than Pt/C and the control sample without the addition of graphene sheets, i.e., Fe-N/C-800, as evidenced by only a slight negative shift (16 mV) of the half-wave potential ($E_{1/2}$) (Figure 4f), which is smaller than that of Pt/C (28 mV) and Fe-N/C-800 (30 mV) modified electrodes. Therefore, the introduction of graphene nanosheets to porous carbons can indeed substantially enhance the durability/stability of the corresponding ORR catalysts.

Because aniline (ANI) has been widely used in the literature to prepare N-doped carbon catalysts for ORR, additional control experiments were also carried out using aniline instead of F2ANI. However, a much lower ORR activity was observed in the corresponding N-C/rGO-800 sample (Figures S17 and S18, Supporting Information), though it was prepared in the same fashion as N-MC/rGO-800, signifying the impacts of polymer morphologies on the formation of mesoporous structures and the eventual ORR activity.

3. Conclusions

In summary, graphene-supported mesoporous carbons with a remarkably high specific surface area as well as rich nitrogen self-doped active sites were successfully prepared by direct pyrolysis of a hybrid precursor composed of GO-supported P2FANI that contained a large amount of amorphous FeOOH in the polymer matrix through an efficient one-pot hydrothermal synthesis. In the carbonization process, the amorphous FeOOH was converted to crystalline Fe_3O_4 nanoparticles that likely acted as rigid templates to prevent the collapse of the polymer matrix. Subsequent evaporation of the volatile iron compounds during P2FANI decomposition and concurrent removal of Fe_3O_4 nanoparticles led to the formation of abundant mesopores. The resulting N-MC/rGO composites exhibited apparent ORR activity in alkaline media, which was primarily ascribed to the rich N dopants. Among the series, the N-MC/rGO-800 samples were identified to be the best catalysts among the series, featuring a more positive onset potential, a much higher diffusion-limited current, a larger number of electron transfer ($n > 3.95$) even at low overpotentials, and stronger tolerance to methanol crossover than state-of-the art commercial Pt/C catalysts. The incorporation of graphene into the hybrids endowed the N-MC/rGO-800 catalyst with markedly enhanced stability, as compared to porous carbons alone and commercial Pt/C. It should be pointed out that although the long-term durability of these catalysts remains to be verified in actual fuel cell devices, the remarkable ORR performance observed in N-MC/rGO-800 strongly suggests the unique potential of the present strategy where graphene-supported nitrogen self-doped mesoporous carbons might be used as promising, efficient, and durable ORR catalysts for PEMFCs.

4. Experimental Section

Synthesis of N-MC/rGO Hybrids: GO nanosheets were first prepared by chemical exfoliation of graphite using the modified Hummers and Offeman's method.[5b,d] 17 mg of GO and 14.8 mmol of $FeCl_3 \cdot 6H_2O$ were then mixed in 20 mL of deionized water, into which was added 1.8 mmol of 2-fluoroaniline (2FANI) under vigorous stirring for about 15 min. The color of the solution changed gradually from yellow to dark brown, signifying the formation of P2FANI. The solution was then transferred to a sealed Teflon-lined autoclave and heated at 180 °C for 4 h. The resulting precipitate (denoted as N-MC/rGO precursor) at the bottom of the autoclave

was collected and dried after washing with copious deionized water. Finally, the dried N-MC/rGO precursor was pyrolyzed at controlled temperatures (300, 500, 700, 800, or 900 °C) for 2 h in an N_2 atmosphere at a gas flow rate of 300 sccm. The final products were referred to as N-MC/rGO-*T* with *T* being the pyrolysis temperature. The procedure was summarized in Scheme 1.

For comparison, a sample was also synthesized via the same procedure as described above except that aniline was used instead of 2-fluoroaniline, and was denoted as N-C/rGO-800. Another comparative sample was prepared in the same manner but without the addition of GO, and referred to as Fe-N/C-800.[8]

Characterization: TEM measurements were conducted on a Tecnai G2-F20 equipped with an EDS detector at an acceleration voltage of 100 kV. The TEM samples were prepared by drop casting a catalyst dispersion directly onto a copper grid coated with a holy carbon film. SEM measurements were conducted with a field-emission scanning electron microscope (S-4800, Hitachi). XPS measurements were performed on a Phi X-tool instrument. Powder XRD patterns were recorded with a Bruker D8-Advance diffractometer using Cu K_α radiation. TGA was performed on a METTLER instruments under an N_2 atmosphere at a heating rate of 5 °C min^{-1}. The BET surface area was determined by Micromeritics ASAP 2010 with nitrogen adsorption at 77 K using the Barrett–Joyner–Halenda (BJH) method. Raman spectra were recorded on a RENISHAW inVia instrument with an Ar laser source of 488 nm in a macroscopic configuration.

Electrochemistry: All electrochemical measurements were performed on a CHI 750E electrochemical workstation (CH Instruments, Chenhua Co., China) in a conventional three-electrode cell, with a platinum wire as the counter electrode, an Ag/AgCl as the reference electrode, and a catalyst-modified glassy-carbon electrode (GCE) as the working electrode. The catalyst ink was prepared by adding 1 mg of a catalyst into a solution containing water, isopropanol, and Nafion (5%) at a volume ratio of 4:1:0.025 to form a homogeneous suspension at the catalyst concentration of 1 mg mL^{-1}. A calculated amount (40 µL) of the suspension was then evenly casted on the clean GCE surface with a syringe and dried in air, corresponding to a catalyst loading of each catalyst at 204 µg cm^{-2}. LSVs were acquired in an O_2-saturated 0.1 M KOH aqueous solution at various rotating speeds (225–2025 rpm).

In the measurements, the Ag/AgCl reference electrode was calibrated with respect to an RHE. The calibration was performed in a high-purity H_2 (99.999%) saturated electrolyte with two Pt wires as the working and counter electrode, respectively. Cyclic voltammograms were acquired at a scan rate of 1 mV s^{-1}, and the average of the two potentials at which the current crossed zero was taken as the thermodynamic potential for the hydrogen electrode reactions. In 0.1 M KOH, $E_{Ag/AgCl} = E_{RHE} + 0.975$ V.

The number of electron transfer (*n*, Equation (1)) and the H_2O_2 yield (Equation (2)) in oxygen reduction were estimated by the following equations

$$n = \frac{4I_{Disk}}{I_{Ring}/N + I_{Disk}} \quad (1)$$

$$H_2O_2\% = \frac{200I_{Ring}/N}{I_{Ring}/N + I_{Disk}} \quad (2)$$

where *N* is the collection efficiency (37%),[8] and I_{Disk} and I_{Ring} are the voltammetric currents at the disk and ring electrodes, respectively.

Supporting Information

Supporting Information is available from the Wiley Online Library or from the author.

Acknowledgements

This work was supported by the National Recruitment Program of Global Experts and the National Natural Science Foundation of China (NSFC 21528301 and NSFC 51402111). L.G.L. also acknowledges financial support from the Scientific Research Foundation for Overseas Chinese Scholar Returnees, State Education Ministry. S.W.C. also thanks the National Science Foundation for partial support of the work (CHE-1265635 and DMR-1409396).

[1] a) X. Q. Huang, Z. P. Zhao, Y. Chen, E. B. Zhu, M. F. Li, X. F. Duan, Y. Huang, *Energy Environ. Sci.* **2014**, *7*, 2957; b) D. S. Geng, Y. Chen, Y. G. Chen, Y. L. Li, R. Y. Li, X. L. Sun, S. Y. Ye, S. Knights, *Energy Environ. Sci.* **2011**, *4*, 760.

[2] a) Z.-Y. Yang, Y.-X. Zhang, L. Jing, Y.-F. Zhao, Y.-M. Yan, K.-N. Sun, *J. Mater. Chem. A* **2014**, *2*, 2623; b) C. He, J. J. Zhang, P. K. Shen, *J. Mater. Chem. A* **2014**, *2*, 3231; c) H.-W. Liang, Z.-Y. Wu, L.-F. Chen, C. Li, S.-H. Yu, *Nano Energy* **2015**, *11*, 366.

[3] a) W. Ding, L. Li, K. Xiong, Y. Wang, W. Li, Y. Nie, S. G. Chen, X. Q. Qi, Z. D. Wei, *J. Am. Chem. Soc.* **2015**, *137*, 5414; b) X. K. Kong, C. L. Chen, Q. W. Chen, *Chem. Soc. Rev.* **2014**, *43*, 2841; c) X. J. Liu, L. G. Li, W. J. Zhou, Y. C. Zhou, W. H. Niu, S. W. Chen, *ChemElectroChem* **2015**, *2*, 803.

[4] a) Y. Y. Shao, G. P. Yin, Y. Z. Gao, *J. Power Sources* **2007**, *171*, 558; b) D. A. Stevens, M. T. Hicks, G. M. Haugen, J. R. Dahn, *J. Electrochem. Soc.* **2005**, *152*, A2309; c) F. Jaouen, E. Proietti, M. Lefevre, R. Chenitz, J. P. Dodelet, G. Wu, H. T. Chung, C. M. Johnston, P. Zelenay, *Energy Environ. Sci.* **2011**, *4*, 114.

[5] a) W. S. H. R. E. Offeman, *J. Am. Chem. Soc.* **1958**, *80*, 1339; b) L. J. Cote, F. Kim, J. X. Huang, *J. Am. Chem. Soc.* **2009**, *131*, 1043; c) S. Stankovich, R. D. Piner, X. Q. Chen, N. Q. Wu, S. T. Nguyen, R. S. Ruoff, *J. Mater. Chem.* **2006**, *16*, 155; d) S. Gilje, S. Han, M. Wang, K. L. Wang, R. B. Kaner, *Nano Lett.* **2007**, *7*, 3394.

[6] a) W. Li, F. Wang, S. S. Feng, J. X. Wang, Z. K. Sun, B. Li, Y. H. Li, J. P. Yang, A. A. Elzatahry, Y. Y. Xia, D. Y. Zhao, *J. Am. Chem. Soc.* **2013**, *135*, 18300; b) Z. S. Wu, S. B. Yang, Y. Sun, K. Parvez, X. L. Feng, K. Mullen, *J. Am. Chem. Soc.* **2012**, *134*, 9082; c) H. X. Zhong, J. Wang, Y. W. Zhang, W. L. Xu, W. Xing, D. Xu, Y. F. Zhang, X. B. Zhang, *Angew. Chem. Int. Ed.* **2014**, *53*, 14235; d) X. D. Zhuang, F. Zhang, D. Q. Wu, N. Forler, H. W. Liang, M. Wagner, D. Gehrig, M. R. Hansen, F. Laquai, X. L. Feng, *Angew. Chem. Int. Ed.* **2013**, *52*, 9668; e) X. D. Zhuang, F. Zhang, D. Q. Wu, X. L. Feng, *Adv. Mater.* **2014**, *26*, 3081; f) W. Wei, H. W. Liang, K. Parvez, X. D. Zhuang, X. L. Feng, K. Mullen, *Angew. Chem. Int. Ed.* **2014**, *53*, 1570.

[7] a) R. Silva, D. Voiry, M. Chhowalla, T. Asefa, *J. Am. Chem. Soc.* **2013**, *135*, 7823; b) C. D. Liang, Z. J. Li, S. Dai, *Angew. Chem. Int. Ed.* **2008**, *47*, 3696.

[8] W. Niu, L. Li, X. Liu, N. Wang, J. Liu, W. Zhou, Z. Tang, S. Chen, *J. Am. Chem. Soc.* **2015**, *137*, 5555.

[9] a) P. Makie, G. Westin, P. Persson, L. Osterlund, *J. Phys. Chem. A* **2011**, *115*, 8948; b) H. P. Cong, X. C. Ren, P. Wang, S. H. Yu, *ACS Nano* **2012**, *6*, 2693.

[10] W. D. Chemelewski, H. C. Lee, J. F. Lin, A. J. Bard, C. B. Mullins, *J. Am. Chem. Soc.* **2014**, *136*, 2843.

[11] a) Y. Zhao, C. G. Hu, Y. Hu, H. H. Cheng, G. Q. Shi, L. T. Qu, *Angew. Chem. Int. Ed.* **2012**, *51*, 11371; b) S. Mao, Z. H. Wen, T. Z. Huang, Y. Hou, J. H. Chen, *Energy Environ. Sci.* **2014**, *7*, 609.

[12] a) Z. L. Li, M. Jaroniec, P. Papakonstantinou, J. M. Tobin, U. Vohrer, S. Kumar, G. Attard, J. D. Holmes, *Chem. Mater.* **2007**, *19*, 3349; b) J. N. Wang, L. Zhang, J. J. Niu, F. Yu, Z. M. Sheng, Y. Z. Zhao, H. Chang, C. Pak, *Chem. Mater.* **2007**, *19*, 453; c) L. Sun, C. G. Tian, M. T. Li, X. Y. Meng, L. Wang, R. H. Wang, J. Yin, H. G. Fu, *J. Mater. Chem. A* **2013**, *1*, 6462; d) L. C. A. Oliveira, E. Pereira, I. R. Guimaraes, A. Vallone, M. Pereira, J. P. Mesquita, K. Sapag, *J. Hazard. Mater.* **2009**, *165*, 87.

[13] M. S. Dresselhaus, A. Jorio, M. Hofmann, G. Dresselhaus, R. Saito, *Nano Lett.* **2010**, *10*, 751.

[14] a) K. L. Ai, Y. L. Liu, C. P. Ruan, L. H. Lu, G. Q. Lu, *Adv. Mater.* **2013**, *25*, 998; b) D. Zhao, J. L. Shui, C. Chen, X. Q. Chen, B. M. Reprogle, D. P. Wang, D. J. Liu, *Chem. Sci.* **2012**, *3*, 3200; c) G. Wu, N. H. Mack, W. Gao, S. G. Ma, R. Q. Zhong, J. T. Han, J. K. Baldwin, P. Zelenay, *ACS Nano* **2012**, *6*, 9764.

[15] R. L. Liu, D. Q. Wu, X. L. Feng, K. Mullen, *Angew. Chem. Int. Ed.* **2010**, *49*, 2565.

[16] H. Kim, K. Lee, S. I. Woo, Y. Jung, *Phys. Chem. Chem. Phys.* **2011**, *13*, 17505.

[17] a) P. J. Wei, G. Q. Yu, Y. Naruta, J. G. Liu, *Angew. Chem. Int. Ed.* **2014**, *53*, 6659; b) Y. Ito, H. J. Qiu, T. Fujita, Y. Tanabe, K. Tanigaki, M. W. Chen, *Adv. Mater.* **2014**, *26*, 4145; c) T. Xing, Y. Zheng, L. H. Li, B. C. C. Cowie, D. Gunzelmann, S. Z. Qiao, S. M. Huang, Y. Chen, *ACS Nano* **2014**, *8*, 6856.

[18] Y. C. Wang, Y. J. Lai, L. Song, Z. Y. Zhou, J. G. Liu, Q. Wang, X. D. Yang, C. Chen, W. Shi, Y. P. Zheng, M. Rauf, S. G. Sun, *Angew. Chem. Int. Ed.* **2015**, *54*, 9907.

[19] a) C. Z. Zhang, N. Mahmood, H. Yin, F. Liu, Y. L. Hou, *Adv. Mater.* **2013**, *25*, 4932; b) C. L. Han, J. Wang, Y. T. Gong, X. Xu, H. R. Li, Y. Wang, *J. Mater. Chem. A* **2014**, *2*, 605.

Received: November 21, 2015
Published online: February 19, 2016